

Supplementary Information

for

**Crystal structure modification enhances air stability and suppresses O₂ evolution in Li₅FeO₄: insights
from experiments and DFT calculations**

Jiasen Wang^a, Xuebao Li^a, Kun Zeng^a, Chao Zhao^a, Zhuangzhi Wu^{a,*}, Dezhi Wang^{a,b*}

^a School of Materials Science and Engineering, Central South University, Changsha 410083, China

^b State Key Laboratory of Powder Metallurgy, Central South University, Changsha 410083, China

Experimental Section

1. Materials Synthesis.

$\text{Li}_{5+x}\text{Fe}_{1-x}\text{Co}_x\text{O}_4$ was prepared via a solid phase sintering process. Stoichiometric amounts of Li_2O (Macklin, 99.99%), Fe_2O_3 (Macklin, 99.95%), and $\text{Co}(\text{OH})_2$ (Macklin, 99.8%) were thoroughly mixed and then molded into 10 mm diameter pellets. The powder underwent calcination at 900 °C for 12 h in a tube furnace under an Ar atmosphere and then promptly transferred to an argon-filled glove box for grinding and storage. Substituted materials were labeled based on their Fe/Co ratio; for instance, LF19C10 represents $x = 0.05$ (Fe/Co = 19/1).

2. Characterization.

The elemental composition of prelithiation powders was determined using inductively coupled plasma optical emission spectroscopy (ICP-OES, Agilent 5110). The crystal structure and phase composition were analyzed by X-ray diffractometer (XRD, Rigaku Mini Flex 600) with Cu-K α radiation ($\lambda = 1.54056 \text{ \AA}$), and structural refinement was performed using GSAS software with the Rietveld method¹. Raman spectroscopy was performed using a Renishaw inVia with an excitation wavelength of 532 nm. The transmission electron microscopy (TEM, FEI Tecnai G2 F20 S-TWIN TMP) was employed to observe the morphology and microstructure, with elemental analysis conducted through energy dispersive spectroscopy (EDS). X-ray photoelectron spectroscopy (XPS, ULVAC-PHI PHI Versa Probe 4) was employed to investigate the electronic information of powders and cathode electrodes. Finally, O_2 release of prelithiated electrode was tested using Differential Electrochemical Mass Spectrometry (DEMS, Linglu QMG220).

3. Electrochemical Measurements.

Prelithiation powders, super P carbon black (SP), and polyvinylidene fluoride (PVDF) were mixed in

N-methyl-2-pyrrolidone (NMP) at a weight ratio of 7:2:1 to fabricate the electrodes. For LiFePO₄-based electrodes with additional prelithated additives (5% of the total mass), the components were combined at a ratio of 8:1:1 for LiFePO₄, SP and PVDF. The resulting slurry was evenly cast onto aluminum foils and dried in a vacuum oven at 100 °C for 10 h. The dried foil was punched into 12 mm round electrodes. A 16 mm lithium metal plate served as the counter electrode, and the CR2025 coin cell was used for assembly. The electrolyte consists of 1 M LiPF₆ dissolved in diethyl carbonate and fluorinated ethylene carbonate (1:1 by volume), with a polyethylene (PE) film serving as the separator. The Si/C anodes were fabricated using the same procedure as the cathodes. Full cells were assembled following the same process as the half-cells, maintaining an N/P ratio of approximately 1.1-1.2.

Charge/discharge measurements were carried out using a multi-channel battery testing system (LAND CT3002A, China) within a voltage window of 2-4.3 V, and the cut-off voltage of the half-cells used for testing prelithated performance was set at 2.5-4.5 V. The electrochemical impedance spectroscopy (EIS) measurements were taken over a frequency range of 0.01-10⁶ Hz with a 0.01 V amplitude, using an electrochemical workstation (Chenhua CHI660E, China).

4. First-principles calculations.

All the calculations were carried out using the density-functional theory (DFT) by Vienna Ab initio simulation package (VASP)² and the projector augmented wave (PAW) method³. The exchange-correlation function was described using the generalized gradient approximation (GGA) in the Perdew-Burke-Ernzerhof (PBE) formulation⁴. The energy cut-off was set at 520 eV, with convergence criteria established at 0.02 eV/Å for force and 10⁻⁴ eV for energy. To correct the strong on-site coulomb interaction of 3d electrons on transition metals, U values of 5.3 eV and 3.32 eV were applied for Fe and Co, respectively⁵.

The Brillouin zone (BZ) was sampled using the Monkhorst-Pack⁶ with a k-point grid size of $4 \times 4 \times 4$ for structural relaxation and $6 \times 6 \times 6$ for density of states (DOS). The diffusion activation energy barriers were calculated by the climbing image nudged elastic band (CI-NEB) method⁷. Three surfaces (001), (220) and (021) were separately constructed to investigate air stability. A 15 Å vacuum layer was introduced in order to prevent interactions between adjacent layers in the surface models. All images of the models were generated by Visualization for Electronic and Structural Analysis (VESTA)⁸.

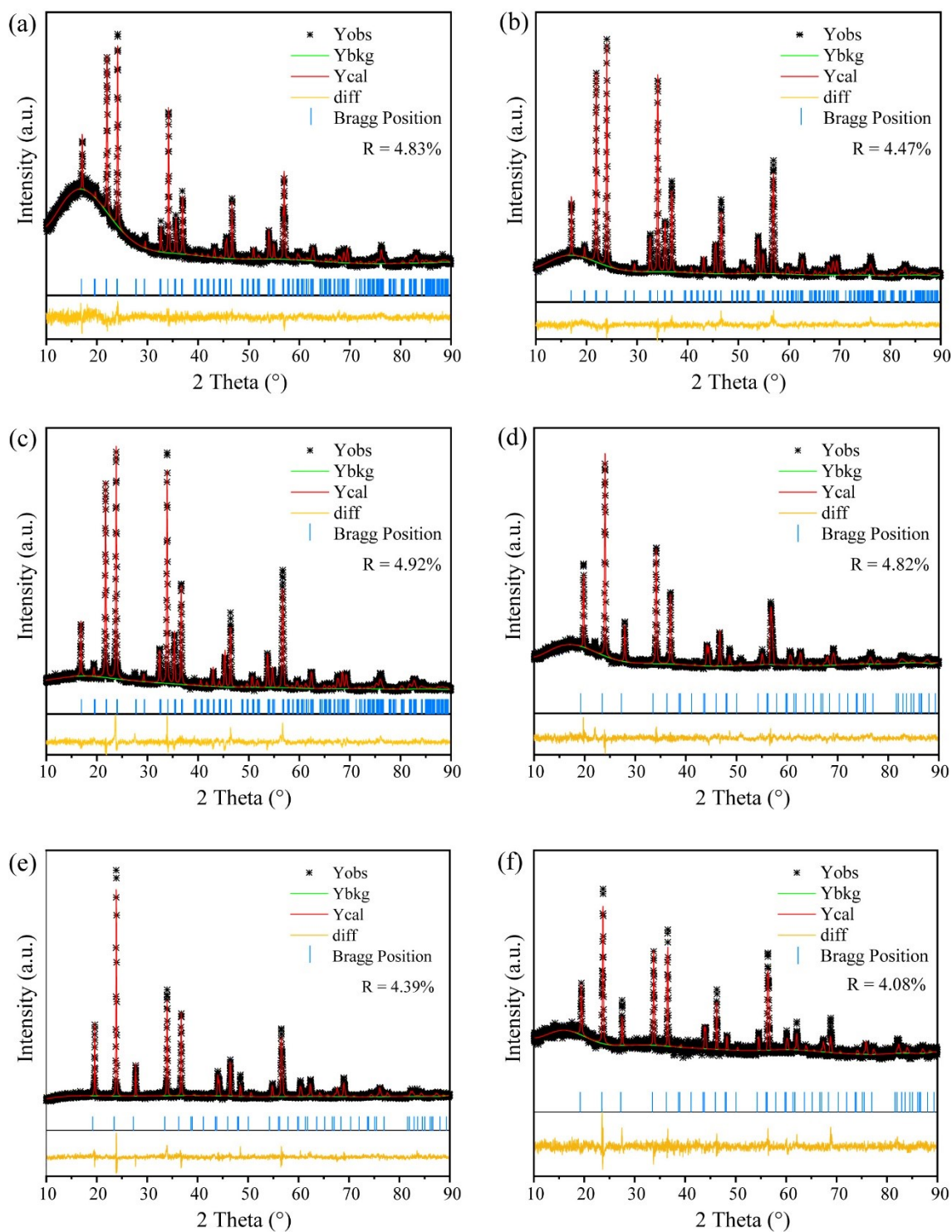


Figure S1 XRD refinement graphs of LFO (a), LF19C10 (b), LF9C10 (c), LF7C10 (d), LF5C30 (e), and LF4C4O (f).

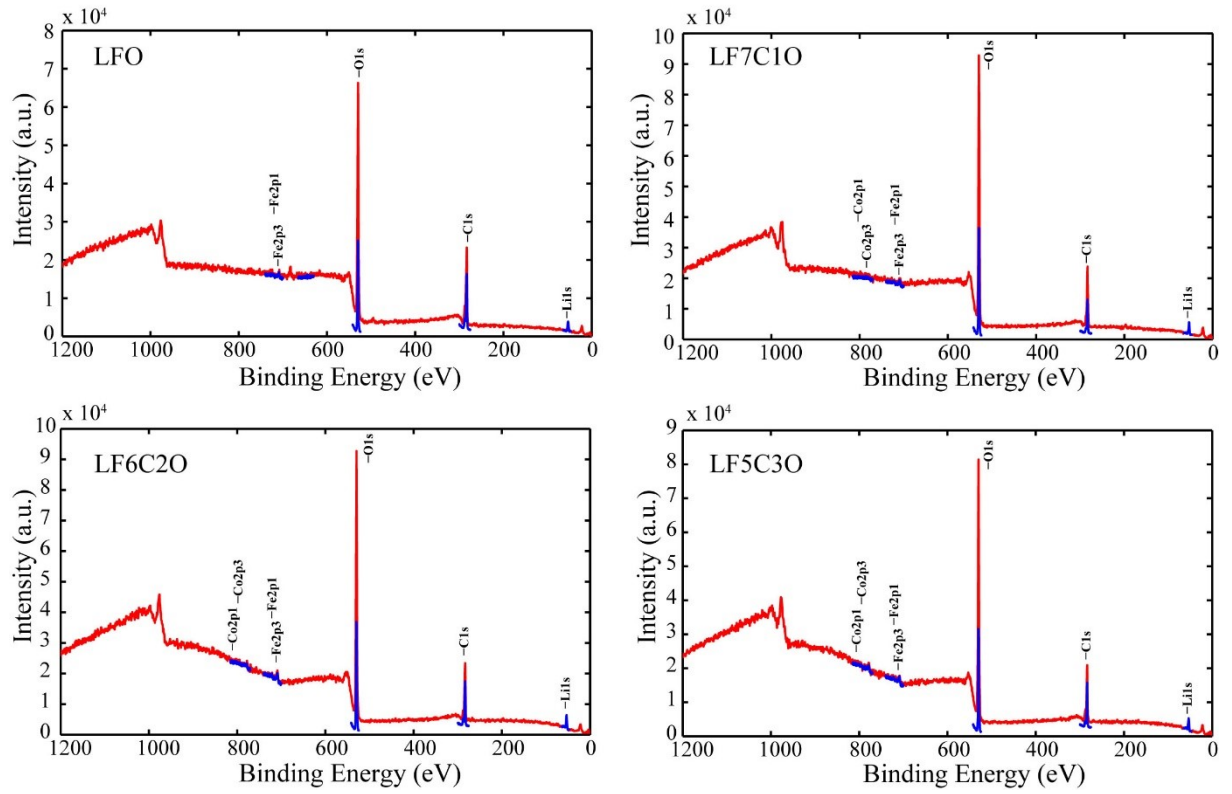


Figure S2 XPS spectra of LFO (a), LF7C10 (b), LF6C20 (c), and LF5C30 (d).

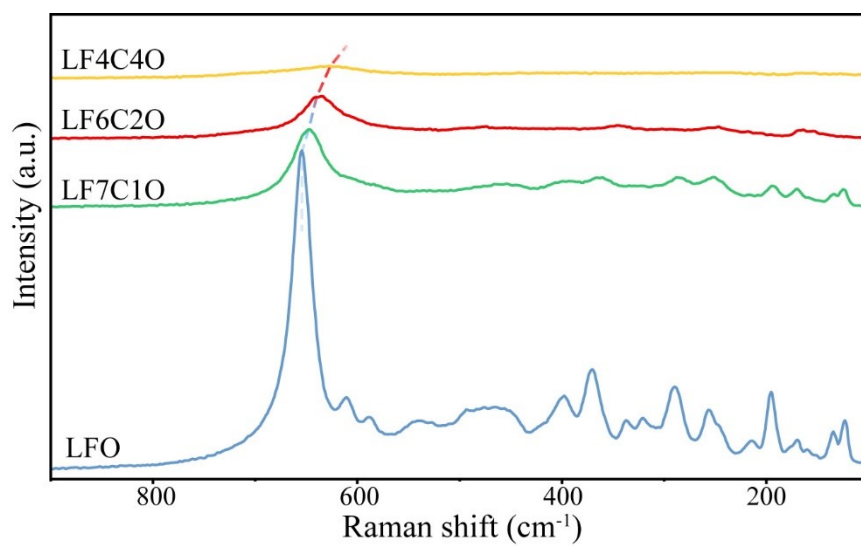


Figure S3 Raman scanning spectrum of LFO, LF7C10, LF6C2O, and LF4C4O.

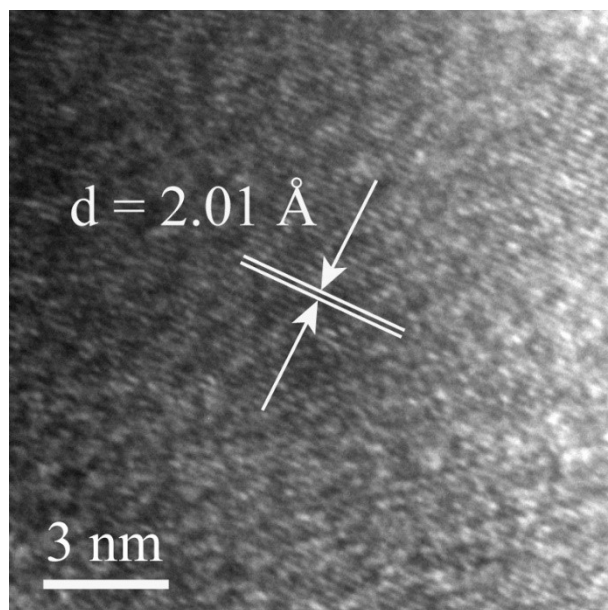


Figure S4 HR-TEM image of LFO.

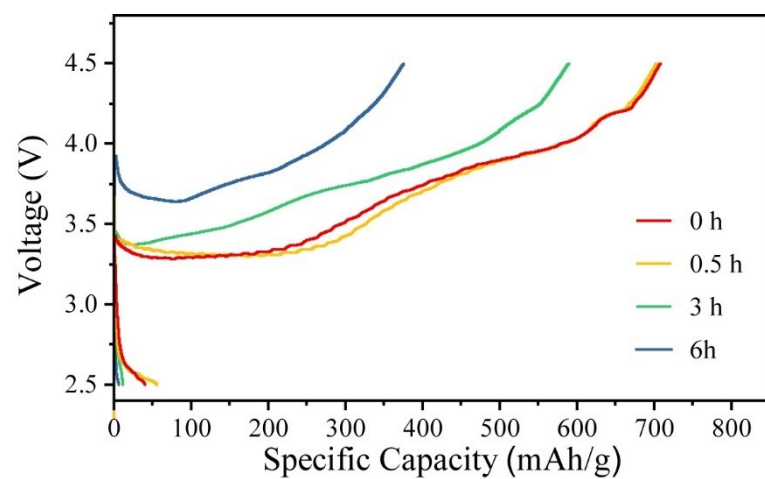


Figure S5 Capacity-voltage curves of LF6C2O exposed to air for different times.

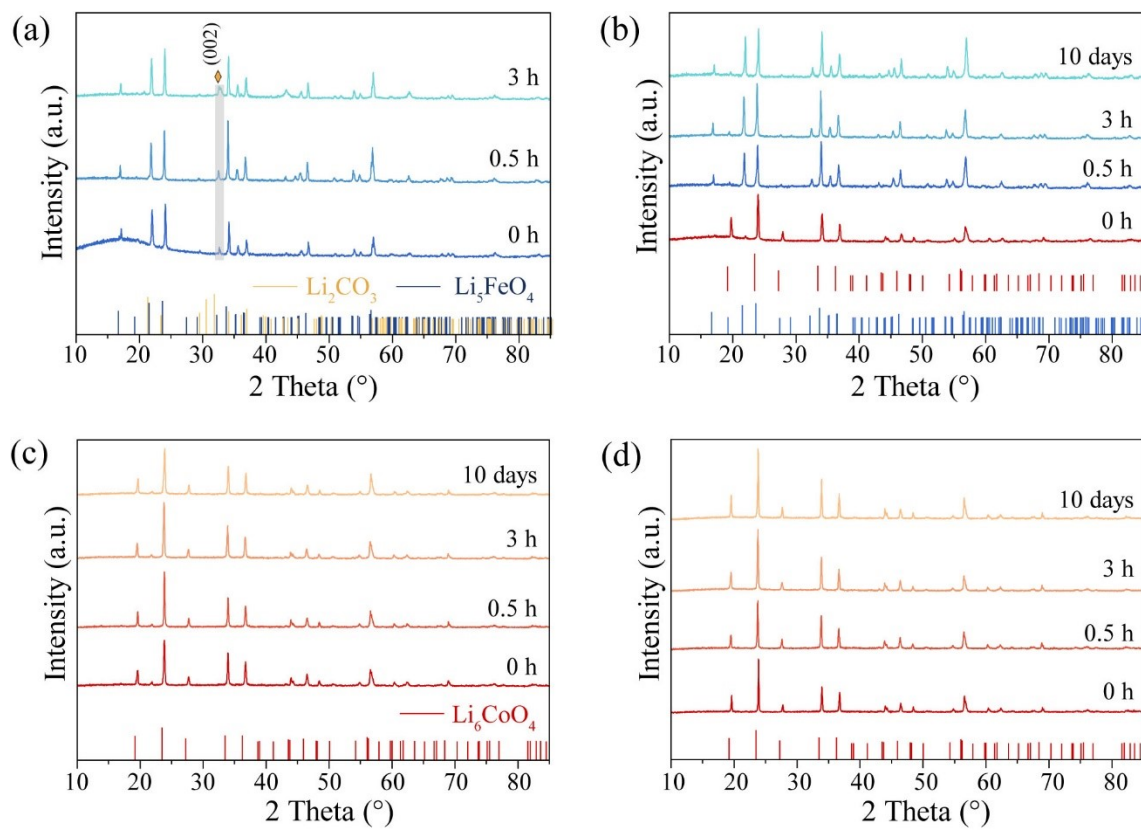


Figure S6 XRD patterns of LFO (a), LF7C1O (b), LF6C2O (c), and LF5C3O (d) exposed to humid air for different times, with LF7C1O, LF6C2O, and LF5C3O after 10 days of storage in a glove box filled with argon.

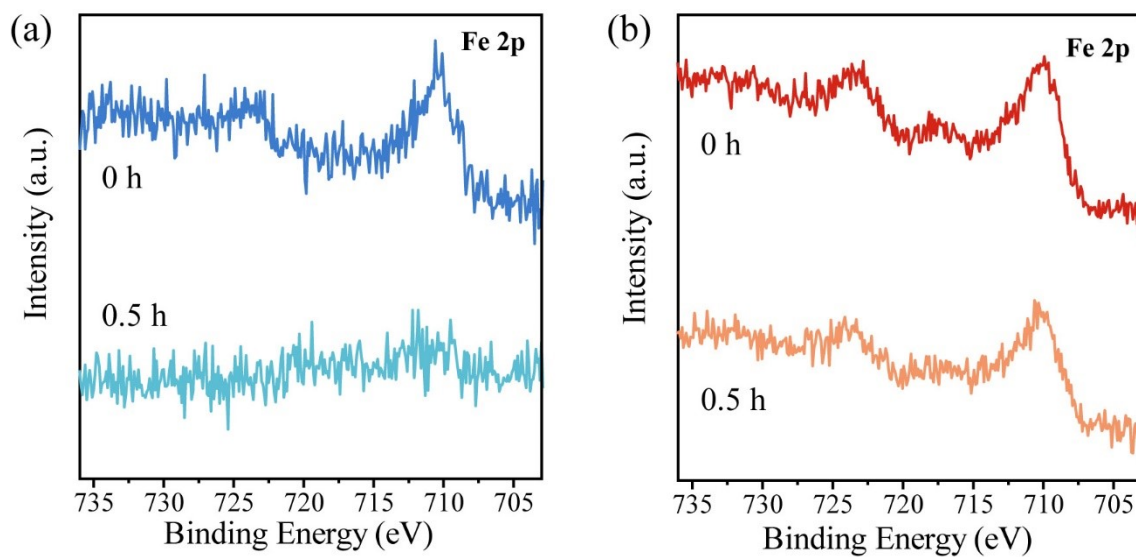


Figure S7 Fe 2p XPS spectrum of LFO (a) and LF6C2O (b) in the pristine state and after 0.5 h exposure to a humid environment.

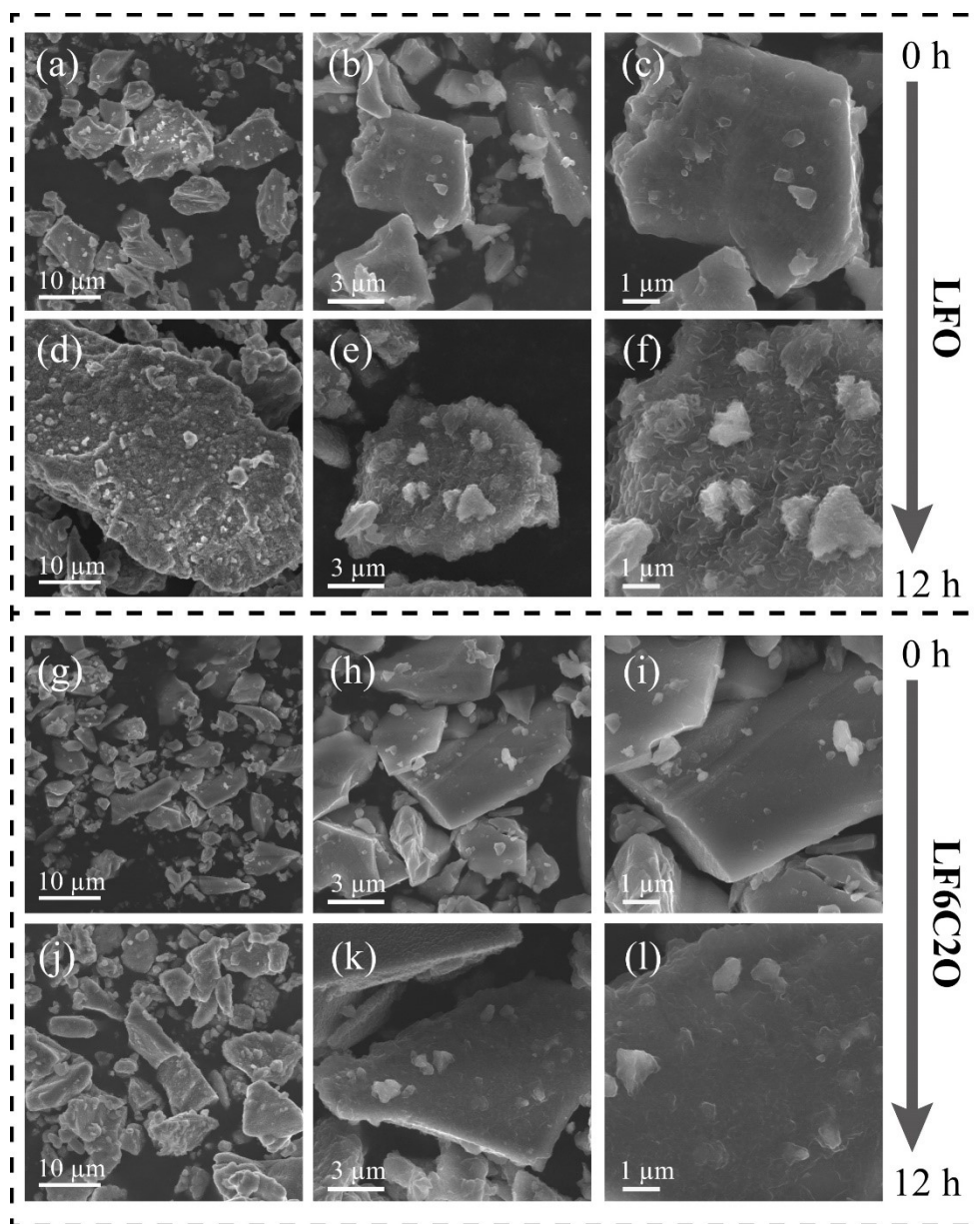


Figure S8 (a-f) SEM images of LFO exposed to air for 0 h (a-c) and 12 h (d-f); (g-l) SEM images of LF6C20 exposed to air for 0 h (g-i) and 12 h (j-l).

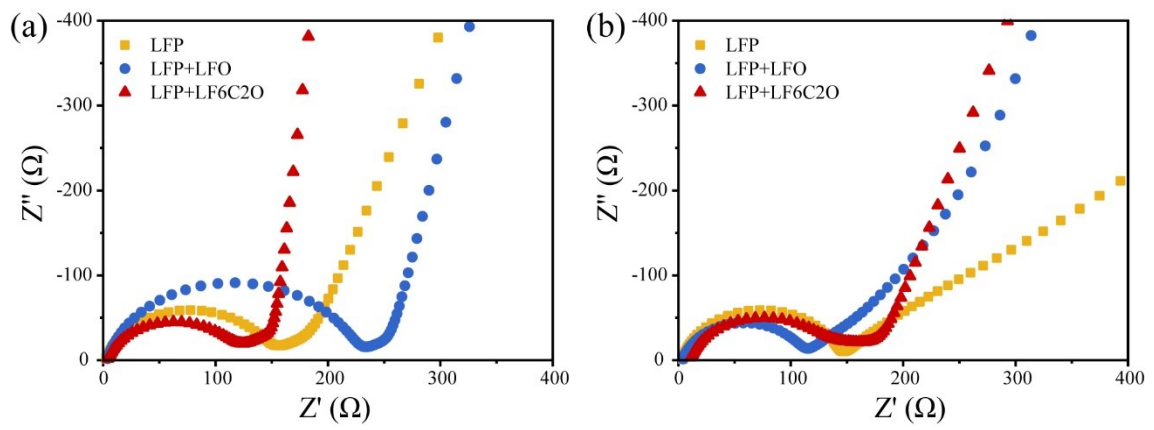


Figure S9 EIS of pristine LFP and prelithiated LFP electrode with different prelithiation materials at before

(a) and after 10 cycles (b).

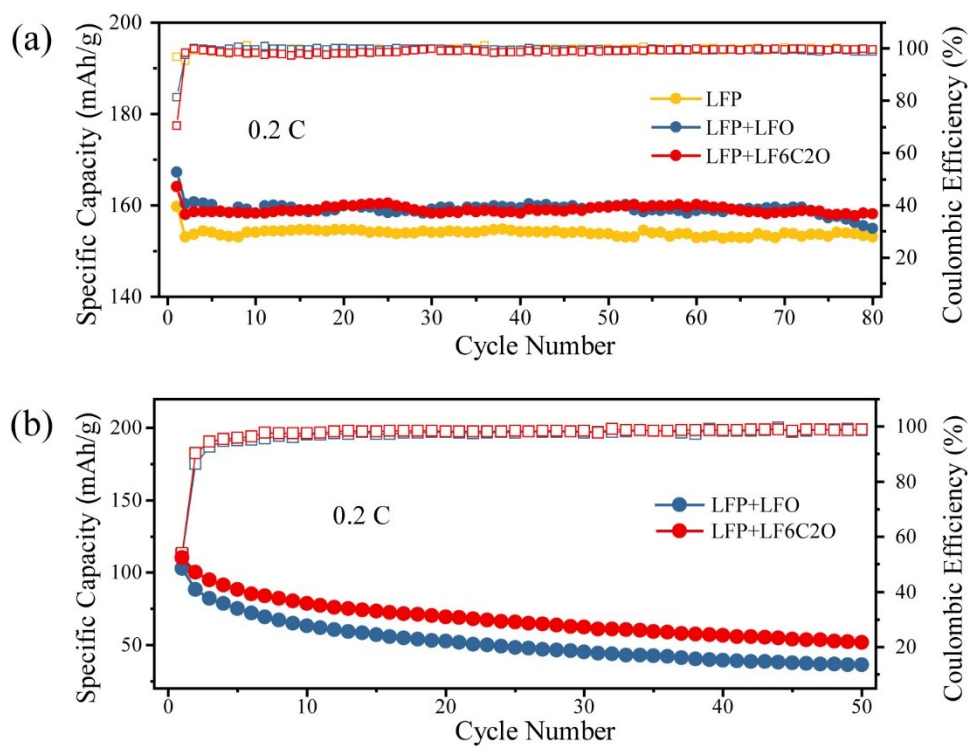


Figure S10 Cycling curves of half-cells (a) and prelithiated LFP||Si/C full-cells (b) at 0.2 C.

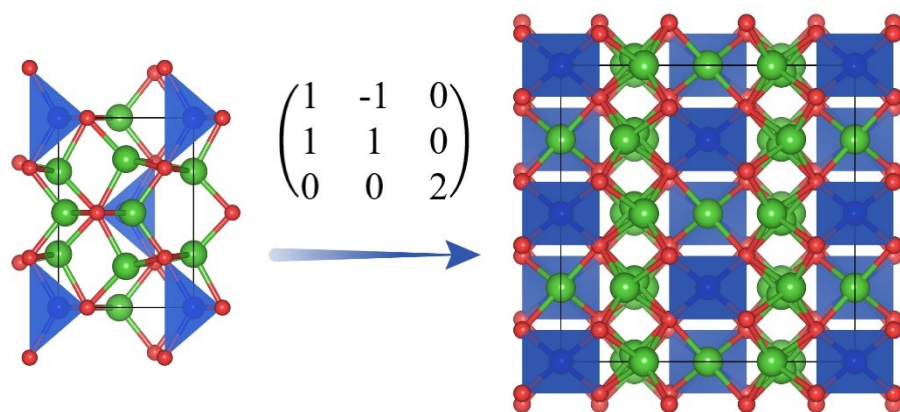


Figure S11 Schematic diagram of Li_6CoO_4 (LCO) primitive unit cell with β -phase (left) and its unit-cell transformation to a supercell (right).

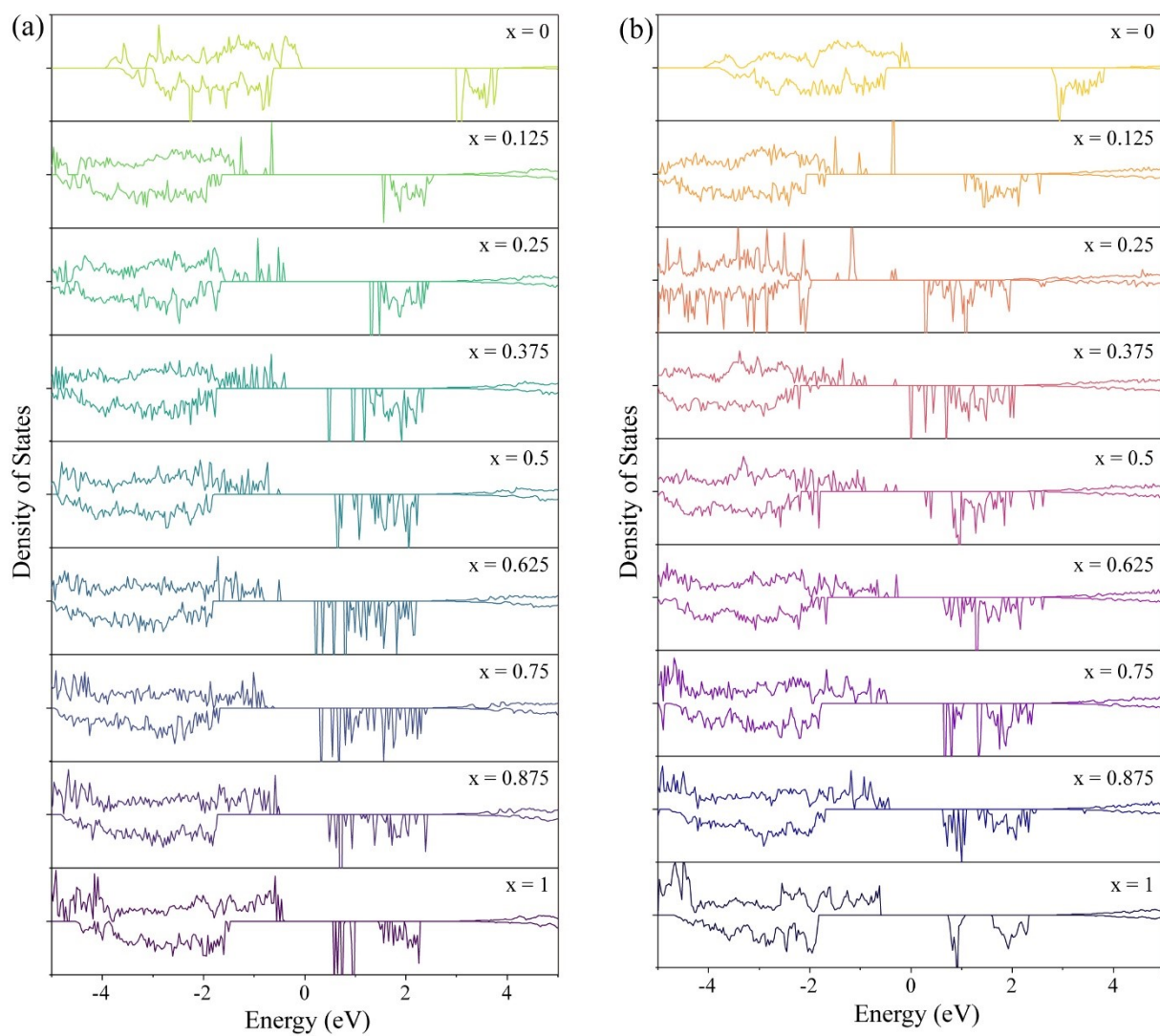


Figure S12 TDOS of α structure (a) and β structure (b) of $\text{Li}_{5+x}\text{Fe}_{1-x}\text{Co}_x\text{O}_4$ with different cobalt content.

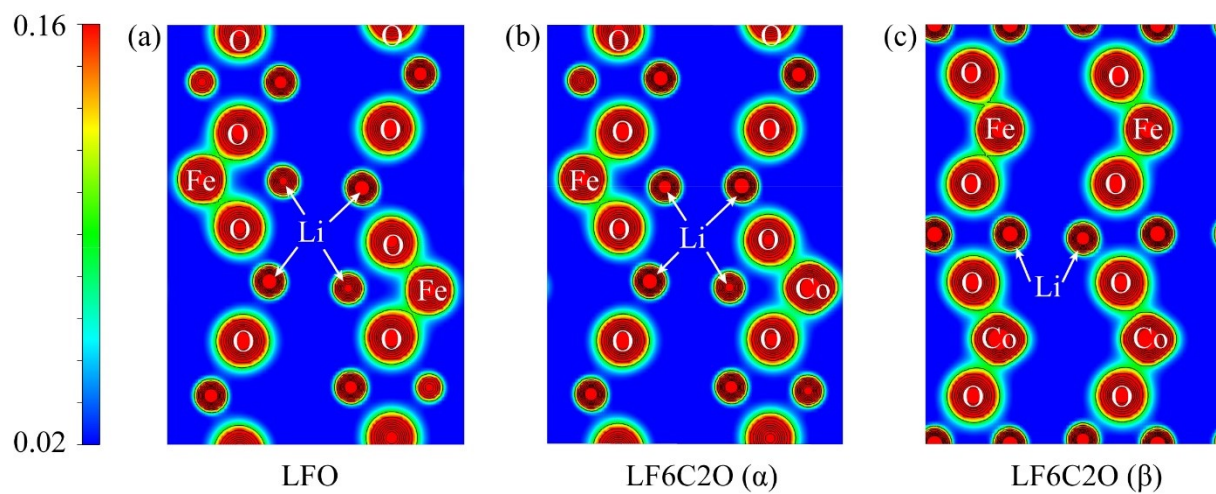


Figure S13 Charge density maps of LFO (a), LF6C2O with α phase (b), and LF6C2O with β phase (c) at (110) plane.

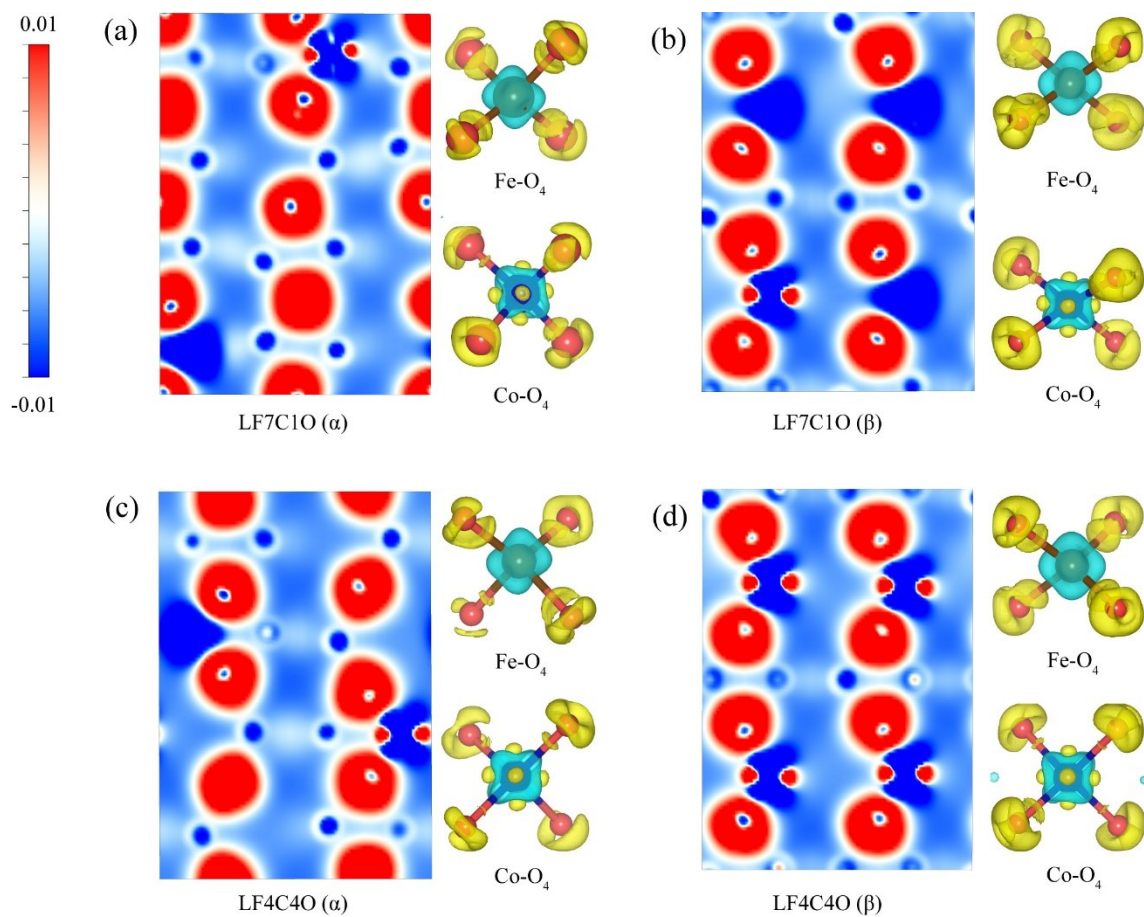


Figure S14 Deformation charge density maps of LF7C1O (a) and LF4C4O (b) at (110) plane for different crystal structures, with their corresponding Fe-O₄ and Co-O₄ tetrahedra.

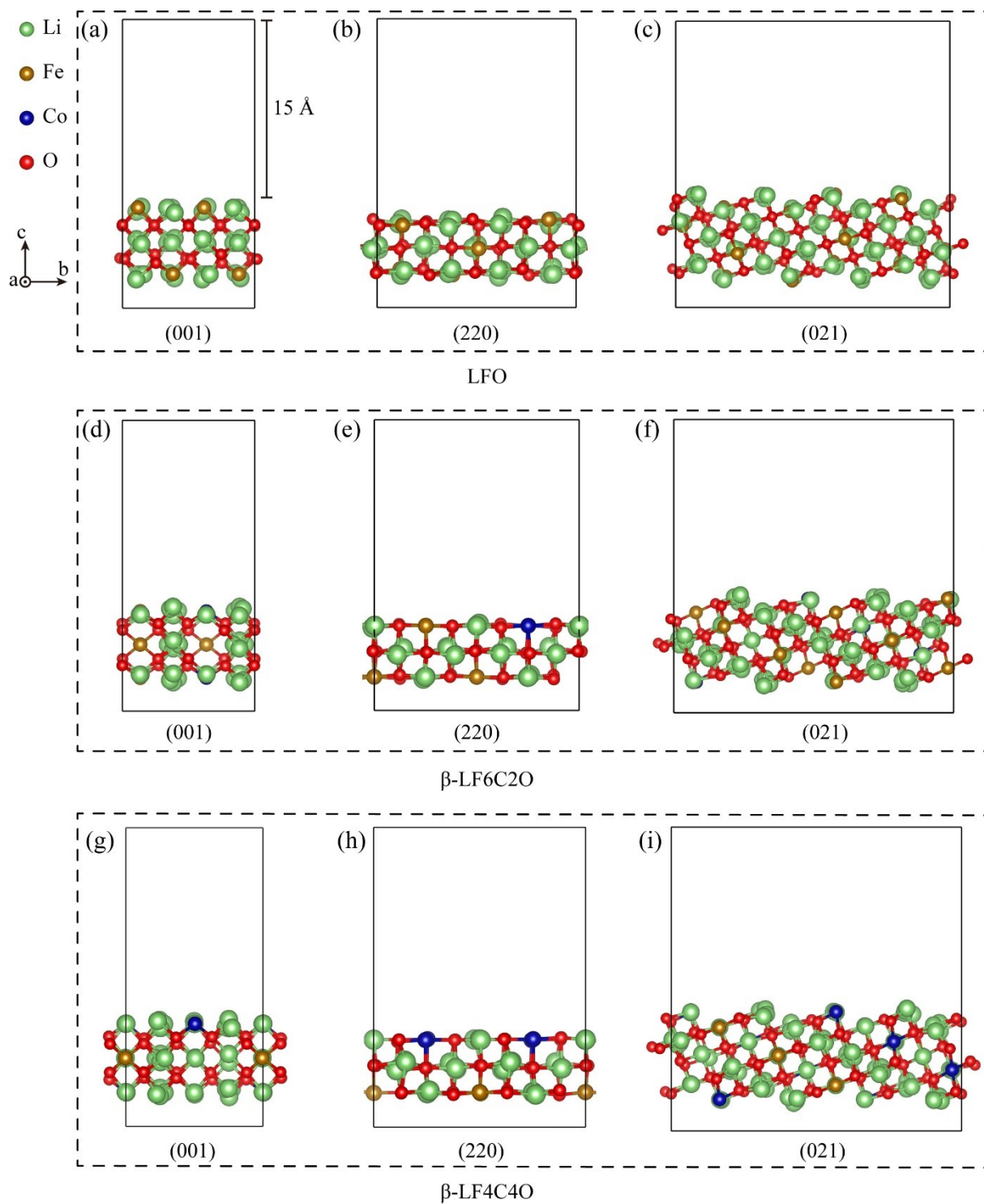


Figure S15 Surface model of adsorption energy of α -phase LFO (a-c), β -LF6C2O (d-f) and β -LF4C4O (g-i)

without structure relaxation.

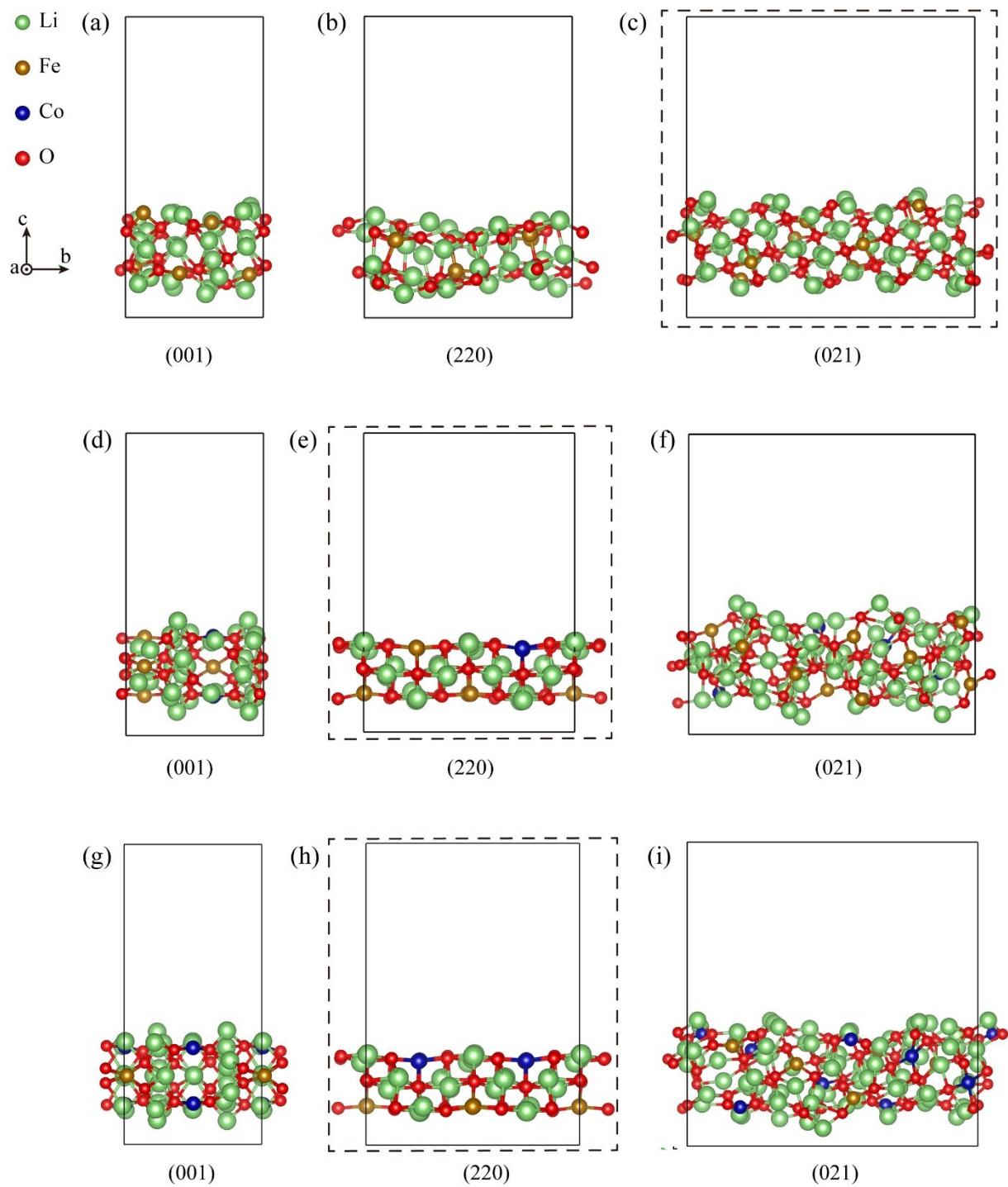


Figure S16 Surface model of adsorption energy of LFO with α -phase (a-c), β -LF6C2O (d-f) and β -LF4C4O (g-i) after structure relaxation calculations.

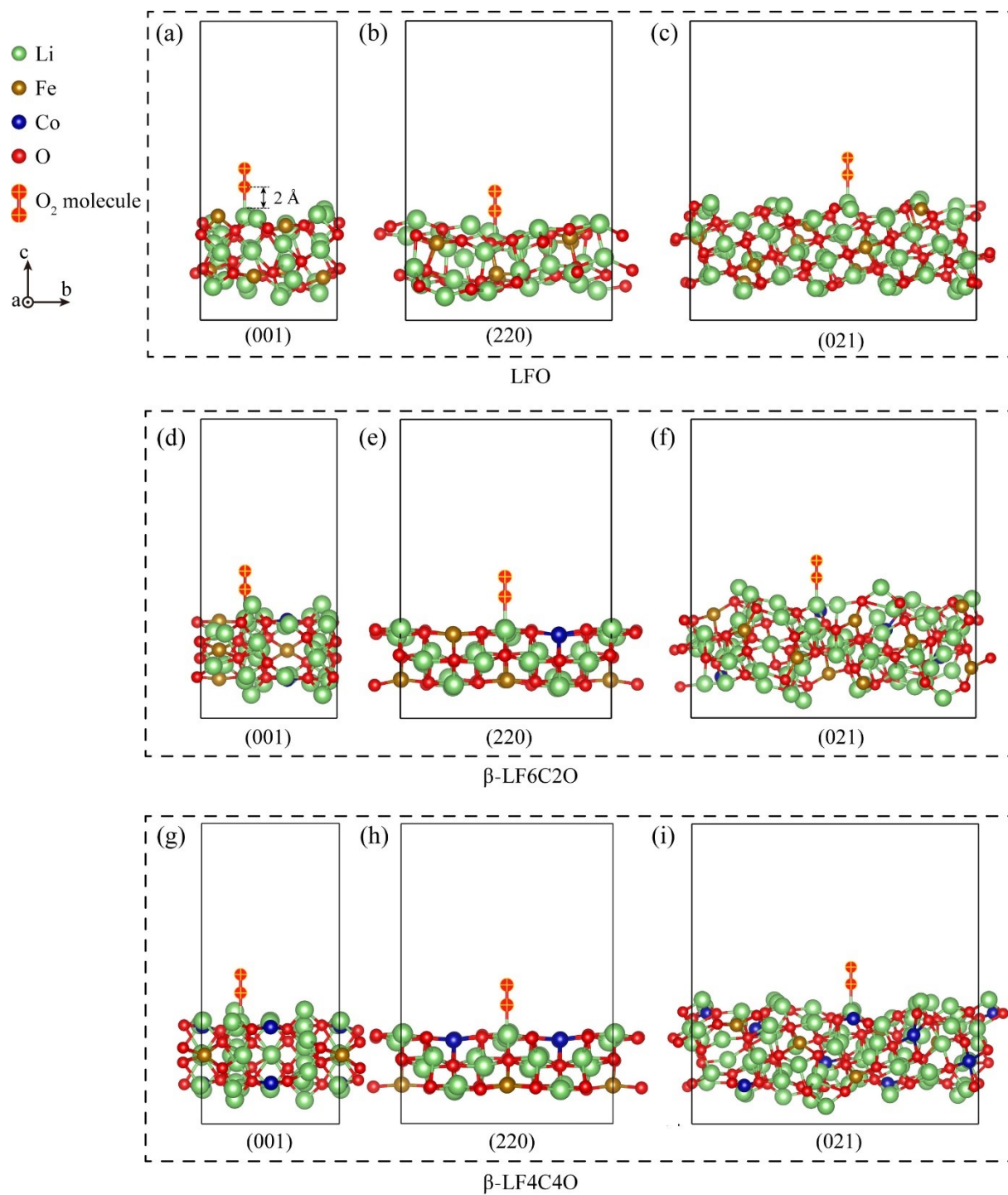


Figure S17 Adsorption configurations of O_2 at the Li site of LFO with α -phase (a-c), β -LF6C2O (d-f) and

β -LF4C4O (g-i).

Table S1 Ratios of elemental compositions for $\text{Li}_{5+x}\text{Fe}_{1-x}\text{Co}_x\text{O}_4$ tested by ICP-OES.

	Li (wt.%)	Fe (wt.%)	Co (wt.%)	Fe/Co (experimental)	Fe/Co (theoretical)
LFO	21.82	34.69	0	1	1
LF19C1O	27.33	33.04	1.81	17.93	19
LF9C1O	27.99	34.54	4.08	8.33	9
LF7C1O	25.45	34.59	5.07	7.19	7
LF6C2O	22.09	25.77	9.19	2.76	3
LF5C3O	22.29	21.28	13.60	1.54	1.67
LF4C4O	22.69	15.40	16.72	0.91	1

Table S2 Refined crystallographic data of $\text{Li}_{5+x}\text{Fe}_{1-x}\text{Co}_x\text{O}_4$ obtained by XRD Rietveld method.

$\text{Li}_{5+x}\text{Fe}_{1-x}\text{Co}_x\text{O}_4$	Structural Parameters			
	a (Å)	b (Å)	c (Å)	V (Å ³)
LFO	9.228	9.214	9.162	779.058
LF19C1O	9.226	9.214	9.164	779.034
LF9C1O	9.222	9.211	9.173	779.139
LF7C1O	6.499	6.499	4.642	196.062
LF6C2O	6.500	6.500	4.638	195.945
LF5C3O	6.516	6.516	4.642	197.086
LF4C4O	6.523	6.523	4.641	197.469

Table S3 Measurement of dissolved transition metals (Fe and Co) in electrolyte from $\text{Li}_{5+x}\text{Fe}_{1-x}\text{Co}_x\text{O}_4$ electrodes by ICP-OES.

	Fe (mg/L)	Co (mg/L)
LFO	31.15	0.09
LF19C1O	11.43	0.67
LF9C1O	9.69	0.61
LF7C1O	17.16	0.03
LF6C2O	0.23	0.01
LF5C3O	0.22	0.01
LF4C4O	33.60	0.16

Table S4 Concentration of LiF, Li₂CO₃, ROCOOLi, and Li₂O on electrode surfaces estimated from Li 1s XPS etching survey.

Etched time	Components (%)	Samples		
		LFP	LFP+LFO	LFP+LF6C2O
Unetched	LiF	22.97	23.56	14.25
	Li ₂ CO ₃	40.28	36.25	62.97
	ROCOOLi	36.75	40.20	22.78
Etched 60 s	LiF	22.10	22.43	38.03
	Li ₂ CO ₃	43.79	44.14	49.67
	ROCOOLi	34.11	21.95	0
	Li ₂ O	0	11.48	12.30

Table S5 Details of lattice constants and formation energies of α -phase obtained by first-principles calculations.

$\text{Li}_{5+x}\text{Fe}_{1-x}\text{Co}_x\text{O}_4$		Structural Parameters			E_f (eV)
x	a (Å)	b (Å)	c (Å)	V (Å ³)	
0	9.17	9.23	9.24	782.52	-1.82
0.125	9.19	9.23	9.27	786.66	-1.79
0.25	9.24	9.24	9.26	790.35	-1.76
0.375	9.28	9.27	9.25	795.54	-1.74
0.5	9.32	9.27	9.24	798.43	-1.72
0.625	9.33	9.29	9.23	800.32	-1.68
0.75	9.34	9.31	9.24	803.72	-1.67
0.875	9.34	9.33	9.24	805.03	-1.66
1	9.34	9.34	9.25	806.60	-1.64

Table S6 Details of lattice constants and formation energies of β -phase obtained by first-principles calculations.

$\text{Li}_{5+x}\text{Fe}_{1-x}\text{Co}_x\text{O}_4$		Structural Parameters			E_f (eV/atom)
x	a (Å)	b (Å)	c (Å)	V (Å ³)	
0	9.17	9.17	9.35	786.89	-1.78
0.125	9.23	9.16	9.34	790.12	-1.77
0.25	9.28	9.22	9.29	794.54	-1.75
0.375	9.23	9.25	9.30	793.86	-1.73
0.5	9.22	9.30	9.30	797.74	-1.71
0.625	9.22	9.29	9.32	798.12	-1.70
0.75	9.20	9.32	9.32	798.42	-1.69
0.875	9.23	9.28	9.32	798.50	-1.68
1	9.25	9.25	9.33	799.51	-1.66

Table S7 Bandgap values of $\text{Li}_{5+x}\text{Fe}_{1-x}\text{Co}_x\text{O}_4$ with different crystal structure obtained by DOS calculations.

$\text{Li}_{5+x}\text{Fe}_{1-x}\text{Co}_x\text{O}_4$	Bandgap (eV)	
	α	β
0	3.025	2.778
0.125	2.153	1.364
0.25	1.677	0.539
0.375	0.825	0.538
0.5	1.080	0.537
0.625	0.669	0.888
0.75	0.890	1.107
0.875	0.949	1.042
1	0.947	1.322

Table S8 Adsorption energies of LFO and LF6C2O on the (001), (220), and (021) surfaces.

	Exposure plane	$E_{\text{ads-O}_2}$ (eV)	$E_{\text{ads-CO}_2}$ (eV)	$E_{\text{ads-H}_2\text{O}}$ (eV)
LFO	(001)	-6.00	-0.24	-0.78
	(220)	-0.88	-0.03	-0.45
	(021)	-3.98	-0.22	-0.69
LF6C2O	(001)	-5.46	-0.27	-0.95
	(220)	-0.72	-0.22	-0.44
	(021)	-2.86	-0.10	-0.63
LF4C4O	(001)	-5.66	-4.10	-0.97
	(220)	-0.77	-0.23	-0.79
	(021)	/	-0.24	/

References

1. S. C. Vogel, *J. Appl. Crystallogr.*, 2011, **44**, 873-877.
2. J. Hafner, *J. Comput. Chem.*, 2008, **29**, 2044-2078.
3. G. Kresse and D. Joubert, *Phys. Rev. B*, 1999, **59**, 1758-1775.
4. J. P. Perdew, K. Burke and M. Ernzerhof, *Phys. Rev. Lett.*, 1996, **77**, 3865-3868.
5. A. Jain, S. P. Ong, G. Hautier, W. Chen, W. D. Richards, S. Dacek, S. Cholia, D. Gunter, D. Skinner, G. Ceder and K. A. Persson, *APL Mater.*, 2013, **1**, 011002.
6. H. J. Monkhorst and J. D. Pack, *Phys. Rev. B*, 1976, **13**, 5188-5192.
7. G. Henkelman, B. P. Uberuaga and H. Jónsson, *J. Chem. Phys.*, 2000, **113**, 9901-9904.
8. K. Momma and F. Izumi, *J. Appl. Crystallogr.*, 2011, **44**, 1272-1276.